






RESEARCH ARTICLE | JANUARY 18 2024

Engineering polar distortions in multiferroic $\text{Sr}_{1-x}\text{Ba}_x\text{MnO}_{3-\delta}$ thin films

Panagiotis Koutsogiannis ; Pedro A. Algarabel ; José A. Pardo ; César Magén  

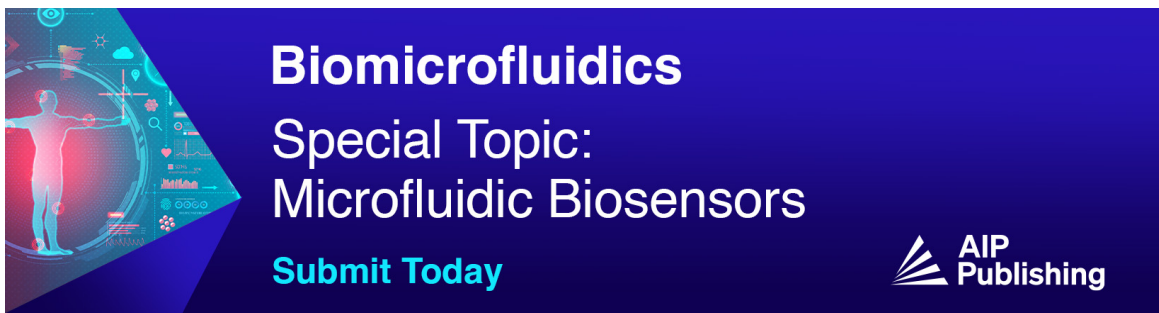


APL Mater. 12, 011113 (2024)
<https://doi.org/10.1063/5.0174793>




CrossMark

19 January 2024 08:28:31



Biomicrofluidics
Special Topic:
Microfluidic Biosensors
Submit Today



Engineering polar distortions in multiferroic $\text{Sr}_{1-x}\text{Ba}_x\text{MnO}_{3-\delta}$ thin films

Cite as: APL Mater. 12, 011113 (2024); doi: 10.1063/5.0174793
Submitted: 2 September 2023 • Accepted: 17 December 2023 •
Published Online: 18 January 2024



Panagiotis Koutsogiannis,^{1,2} Pedro A. Algarabel,^{1,2} José A. Pardo,^{1,3,4} and César Magén^{1,2,a)}

AFFILIATIONS

¹Instituto de Nanociencia y Materiales de Aragón (INMA), CSIC-Universidad de Zaragoza, 50009 Zaragoza, Spain

²Departamento de Física de la Materia Condensada, Universidad de Zaragoza, 50018 Zaragoza, Spain

³Laboratorio de Microscopías Avanzadas (LMA), Universidad de Zaragoza, 50018 Zaragoza, Spain

⁴Departamento de Ciencia y Tecnología de Materiales y Fluidos, Universidad de Zaragoza, 50018 Zaragoza, Spain

^{a)} Author to whom correspondence should be addressed: cmagend@unizar.es

ABSTRACT

The physical properties of perovskite oxide thin films are governed by the subtle interplay between chemical composition and crystal symmetry variations, which can be altered by epitaxial growth. In the case of perovskite-type multiferroic thin films, precise control of stoichiometry and epitaxial strain allows for gaining control over the ferroic properties through selective crystal distortions. Here, we demonstrate the chemical tailoring of the polar atomic displacements by tuning the stoichiometry of multiferroic $\text{Sr}_{1-x}\text{Ba}_x\text{MnO}_{3-\delta}$ ($0 \leq x \leq 0.5$) epitaxial thin films. A combination of x-ray diffraction and aberration-corrected scanning transmission electron microscopy enables unraveling the local polarization orientation at the nanoscale as a function of the film's composition and induced crystalline structure. We demonstrate experimentally that the orientation of polarization is intimately linked to the Ba doping and O stoichiometry of the films and, with the biaxial strain induced by the substrate, it can be tuned either in-plane or out-of-plane with respect to the substrate by the appropriate choice of the post-growth annealing temperature and O_2 atmosphere. This chemistry-mediated engineering of the polarization orientation of oxide thin films opens new venues for the design of functional multiferroic architectures and the exploration of novel physics and applications of ferroelectric textures with exotic topological properties.

© 2024 Author(s). All article content, except where otherwise noted, is licensed under a Creative Commons Attribution (CC BY) license (<http://creativecommons.org/licenses/by/4.0/>). <https://doi.org/10.1063/5.0174793>

I. INTRODUCTION

Multiferroic magnetoelectric materials present exciting fundamental physics¹ and appealing functional properties.² The coexistence of magnetic and polar orders, and the emergence of coupling between them, have compelled the scientific community to explore new pathways toward their applications in diverse technologies, such as low-power data storage and memories,^{3–5} energy storage and photovoltaics,^{6–8} and neural networks.⁹ Of particular interest are multiferroic oxides comprising the ABO_3 perovskite structure, which offer a plethora of physical phenomena driven by small variations of stoichiometry and crystal symmetry.^{2,9} Thin films present additional degrees of freedom, which can be explored in the quest for new multiferroic materials, such as low dimensionality or substrate-induced strain.^{10,11} In many perovskite thin films, such as SrTiO_3 ,¹² EuTiO_3 ,¹³ or KTaO_3 ,¹⁴ epitaxial strain can induce

ferroelectricity by coupling with soft phonon modes, which stabilizes lower-symmetry, non-centrosymmetric phases.¹⁵ Similarly, magnetoelectric effects can emerge under epitaxial strain or chemical pressure, due to the strong coupling between lattice, charge, spin, and orbital degrees of freedom, which exists when the B cation has partially filled $3d^n$ orbitals.^{16,17} Particularly, antiferromagnetic materials can show prominent magnetoelectric coupling under biaxial strain by suppressing the antiferromagnetic exchange interaction as a consequence of ionic displacements.¹⁸

An exciting family of multiferroics is AMnO_3 ($A = \text{Ca}, \text{Sr}, \text{Ba}$) perovskite. These are antiferromagnets¹⁸ or weak ferromagnets,¹⁹ presenting ferroelectricity²⁰ driven by the off-centering of the magnetic Mn^{4+} . The first-principles calculations of Bhattacharjee *et al.*²¹ predicted the emergence of a multiferroic state in CaMnO_3 upon mechanical or chemical strain engineering. Günter *et al.*²⁰ provided experimental evidence of incipient ferroelectricity in epitaxially

strained CaMnO_3 films grown on LaAlO_3 substrates. Lee and Rabe²² also predicted the multiferroic nature of cubic SrMnO_3 under strain, while soon after, Becher *et al.*²³ unraveled its polar nature using temperature-dependent second harmonic generation. Recently, the ferroelectric nature of SrMnO_3 thin films has been experimentally demonstrated at low temperatures (10 K),²⁴ while room-temperature ferroelectricity has been accessible via selective oxygen annealing.²⁵ A remarkable advance was the room-temperature stabilization of the ferroelectric perovskite phase in $\text{Sr}_{1-x}\text{Ba}_x\text{MnO}_3$ single crystals ($x \geq 0.45$) evidenced by ferroelectric hysteresis at 2 K.²⁶ Bulk $\text{Sr}_{1-x}\text{Ba}_x\text{MnO}_3$ in thermodynamic equilibrium shows the hexagonal 4H structure, while a cubic perovskite polymorph appears above 1400 °C only for low Ba contents ($x \leq 0.15$).²⁷ Different strategies have been followed to prepare the metastable perovskite phase at room temperature up to $x = 0.5$, having lattice parameters between 3.806 Å ($x = 0$) and ~ 3.90 Å ($x = 0.5$).^{26,28} Langenberg *et al.*²⁹ showed that $\text{Sr}_{1-x}\text{Ba}_x\text{MnO}_{3-\delta}$ (SBMO, $0 \leq x \leq 0.5$) epitaxial thin films with pseudocubic (tetragonally distorted cubic) structure can be grown on several perovskite substrates under the appropriate experimental conditions and below a critical film thickness. Those films were coherently strained and had a lattice mismatch with the substrate ranging between 0% and 4%, which paved the way for epitaxial strain engineering of this family. For a particular substrate, the strain of the films can be tuned from tensile to compressive and change its magnitude by modifying the Ba content and the concentration of oxygen vacancies.²⁹

The polar nature of SrMnO_3 thin films has been widely studied by scanning transmission electron microscopy and second harmonic generation, while electrical and magnetic properties have been investigated by spectroscopy and scanning probe microscopy techniques among others.^{23,30–32} In SrMnO_3 films under tensile epitaxial strain, the polar displacements occur along the in-plane $\langle 110 \rangle$ pseudocubic crystal directions, and the formation of polar domains has been evidenced.²³ Furthermore, polar gradients can emerge via the modulation of strain and oxygen content.³⁰ However, the impact of Ba and O content on the type of polar displacements as well as the structural and electrical properties of $\text{Sr}_{1-x}\text{Ba}_x\text{MnO}_{3-\delta}$ films has drawn little attention so far.

In the present work, we deposited epitaxial $\text{Sr}_{1-x}\text{Ba}_x\text{MnO}_{3-\delta}$ thin films using targets with different Ba contents ($0 \leq x \leq 0.5$) and various post-annealing conditions (O_2 pressure, substrate temperature) to regulate the concentration of oxygen vacancies (δ) of the films. Scanning transmission electron microscopy was utilized to comprehensively examine the impact of Ba content and O stoichiometry on the polar atomic displacements in biaxial

strained films on single-crystalline substrates. Our results evidence a chemistry-mediated control of the polar states observed in these films. The magnitude and orientation of the polar displacements can be tuned by the Ba content and the O stoichiometry from in-plane to out-of-plane with respect to the substrate. Finally, we show that polar displacements are highly dependent on the cooperative effects between the growth parameters that can be refined desirably, smoothing the path toward new tailored multiferroic architectures.

II. RESULTS AND DISCUSSION

SBMO films synthesized under various conditions were investigated. The effects of different Ba and O content on the crystalline structure of the films were studied both separately and jointly. The starting point was the growth of $\text{Sr}_{1-x}\text{Ba}_x\text{MnO}_{3-\delta}$ ($0 \leq x \leq 0.5$) films with the best crystal quality and the highest oxygen content. Then, the impact of Ba doping on the crystal structure and the atomic displacements was investigated in these samples. Next, we varied the annealing conditions (O_2 pressure and substrate temperature) to deliberately induce oxygen vacancies in the films and evaluate their effect on the crystal structure down to the atomic scale. For the sake of simplicity, the role of each growth or post-growth parameter will be discussed separately, to conclude with a discussion on the combined effects of both variables.

A. Effect of Ba content

$\text{Sr}_{1-x}\text{Ba}_x\text{MnO}_{3-\delta}$ ($x = 0, 0.4$, and 0.5) thin films were grown on LSAT substrates using different *in situ* annealing conditions depending on the Ba content. X-ray diffraction (XRD) was used to refine the optimized growth conditions (see Fig. S3 of the supplementary material) and to determine the samples with the best crystal quality and the maximum oxygen content, which were selected for further characterization. The optimal annealing parameters, listed in Table I, were influenced by the Ba doping and strain, since both favor the formation of oxygen vacancies as a countermeasure against the expanded cell volume.³³ Film thickness values were $t = 18$ nm for $x = 0$, $t = 11$ nm for $x = 0.4$, and $t = 7$ nm for $x = 0.5$, selected just below the critical thickness estimated by Langenberg *et al.*²⁹ Symmetric $\theta/2\theta$ scans were performed to analyze the effect of the chemical substitution of Sr with the larger Ba cation on the out-of-plane lattice parameter. Figure 1(a) shows the $\theta/2\theta$ scans in the vicinity of the 002 LSAT peak in the three films with different compositions ($x = 0, 0.4$, and 0.5), prepared under the annealing

TABLE I. Annealing conditions and main structural parameters of optimized SBMO films as a function of the Ba content (x): annealing temperature (T_{ann}), annealing O_2 pressure (P_{ann}), thickness (t), out-of-plane lattice parameter (c), out-of-plane strain (ϵ_{zz}) calculated as $100 \times (c_{\text{film}} - c_{\text{bulk}})/c_{\text{bulk}}$, in-plane lattice parameter (a), in-plane strain (ϵ_{xx}) calculated as $100 \times (a_{\text{film}} - a_{\text{bulk}})/a_{\text{bulk}}$, ratio between out-of-plane and in-plane lattice parameter (c/a), and cell volume (V).

x	T_{ann} (°C)	P_{ann} (Torr)	t (nm)	c (Å)	ϵ_{zz}	a (Å)	ϵ_{xx}	c/a	V (Å ³)
0	800	500	18	3.76(1)	−1.2%	3.868	+1.6%	0.972(3)	56.2(2)
0.4	350	590	11	3.84(2)	−0.4%	3.868	+0.3%	0.993(6)	57.5(3)
0.5	650	350	7	3.93(4)	+0.8%	3.868	+0.3%	1.02(1)	58.8(6)

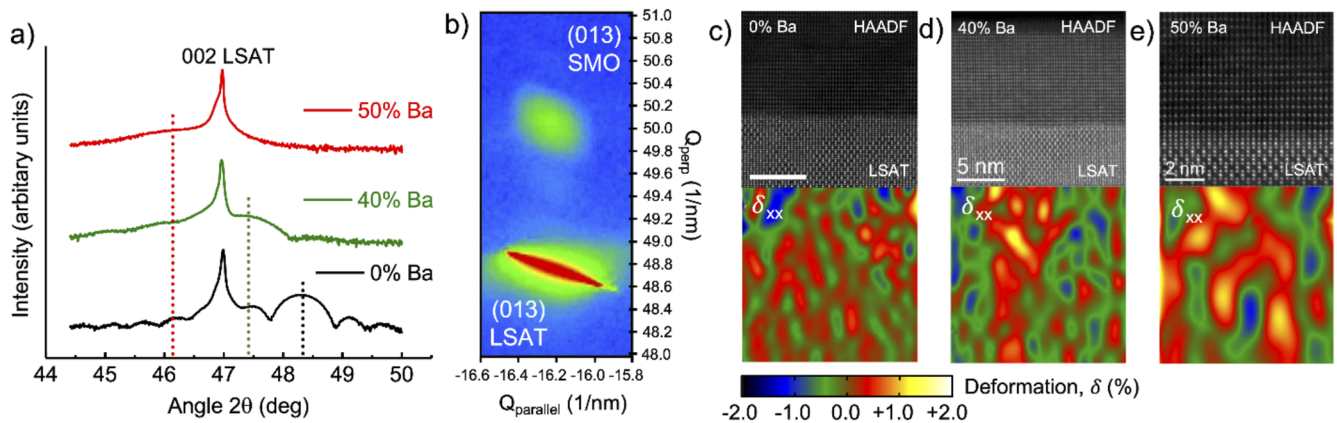


FIG. 1. (a) Symmetric $\theta/2\theta$ x-ray diffraction scans of 18 nm-thick $\text{SrMnO}_{3-\delta}$ (0% Ba), 11 nm-thick $\text{Sr}_{0.6}\text{Ba}_{0.4}\text{MnO}_{3-\delta}$ (40% Ba) and 7 nm-thick $\text{Sr}_{0.5}\text{Ba}_{0.5}\text{MnO}_{3-\delta}$ (50% Ba) epitaxial films synthesized on LSAT (001) with the annealing parameters listed in Table I. The position of the 002 reflection in each film (dashed lines) shifts toward smaller 2θ angles with increasing Ba content. In the case of 50% Ba, the peak of the film is on the left side of the peak of the substrate, indicating that the out-of-plane lattice parameter of $\text{Sr}_{0.5}\text{Ba}_{0.5}\text{MnO}_{3-\delta}$ is larger than that of LSAT. (b) XRD reciprocal space map of the 0% Ba film in the vicinity of the 013 reflection. (c)–(e) (110) cross-sectional STEM-HAADF images and their corresponding in-plane (δ_{xx}) deformation maps relative to the LSAT substrate, calculated by GPA. The three deformation maps indicate fully coherent growth and no strain relaxation along the film thickness.

conditions shown in Table I. The position of the 002 SBMO film peak shifts toward smaller 2θ angles upon increasing the Ba content, showing an increase of the out-of-plane lattice parameter. The width of the peaks increases with decreasing film thickness, according to Scherrer's equation. Von Laue oscillations are visible at both sides of the main reflection in the films with $x = 0$ and $x = 0.4$, proving their high crystal quality, while their absence in $x = 0.5$ is a consequence of the reduced film thickness. Reciprocal space maps (RSM) were collected to analyze the degree of strain induced by the substrate. As shown in Fig. 1(b) for the parent compound SrMnO_3 , the coincidence of the in-plane component of the reciprocal space vector of the 013 asymmetric reflection of both film and substrate evidence that the epitaxial film is fully strained. Similar RSM experiments in $x = 0.4$ and $x = 0.5$ films yielded inconclusive results due to the poor visibility of the film's peak in thinner films. Coherent growth was confirmed in these films by an alternative, local structural analysis performed by aberration-corrected scanning transmission electron microscopy (STEM). Geometrical phase analysis (GPA, see the Experimental section) of the cross-sectional high-angle annular dark field (HAADF) images of the three films was performed to determine the relationship between the lattice parameters of the film and the substrate, as depicted in Figs. 1(c)–1(e). The in-plane lattice parameter remains constant (within a statistical error of 0.05%) across the interface between the film and the substrate. Thus, the out-of-plane lattice parameter (c), the c/a ratio, and the cell volume listed in Table I could be determined from the XRD and STEM analysis shown in Fig. 1 for the $x = 0, 0.4$, and 0.5 films. This summary allows us to conclude that, together with the out-of-plane lattice parameter, the cell volume also increases, as should be expected, by doping with the larger Ba cation. This trend might affect the kind of polar displacements occurring in these films.

While for $x = 0.4$ the SBMO film still grows under slight tensile strain, in the case of the highest Ba content ($x = 0.5$), the out-of-plane lattice parameter increases drastically, the c/a ratio

becomes larger than unity, and thus compressive strain emerges. This extensive increase occurs even though Ba content rises only 10%, signifying the impact of the low-oxygen annealing conditions (compared to $x = 0$ and 0.4 films) on the cell volume. According to theoretical predictions, the phase diagrams of epitaxial ferroelectric thin films are bound to mechanical boundary conditions, absent in free crystals, which may trigger phases that are hindered in the bulk.³⁴ Moreover, first-principles studies of epitaxial strain in perovskites indicate that the change from tensile to compressive strain can induce a rotation of the polarization from the in-plane to the out-of-plane direction.^{15,34} Hence, it is plausible that, in our SBMO films for $x = 0.5$, polar displacements relocate (relative to $x = 0.4$) toward a non-centrosymmetric out-of-plane configuration. Figure 2 shows atomic-resolution annular bright field (ABF) STEM images of cross-sectional specimens of the SrMnO_3 and $\text{Sr}_{0.5}\text{Ba}_{0.5}\text{MnO}_{3-\delta}$ films, grown in the optimal conditions (Table I), observed along the [110] zone axis. The images were taken at the interfaces between the LSAT substrates and the films. In ABF configuration, both the cation and the oxygen sublattices can be visualized simultaneously.³⁵ Polar displacements previously observed in epitaxial SrMnO_3 films along the $\langle 110 \rangle$ directions^{23,30} are confirmed in this case. Oxygen shifts are predominantly in-plane, with an average displacement of ~ 8 pm with respect to the centrosymmetric positions. However, Mn shifts of ~ 7 pm in-plane are limited to the interfacial region, whereas out-of-plane displacements are negligible within the margins of error. On the other hand, in the case of $\text{Sr}_{0.5}\text{Ba}_{0.5}\text{MnO}_{3-\delta}$, oxygen out-of-plane displacements are dominant with values of ~ 15 pm, whereas minor in-plane displacements of ~ 5 pm were detected. Atomic displacements observed in the LSAT substrate, which is a cubic centrosymmetric crystal, are associated with other experimental factors such as interfacial strain and a slight mistilt with respect to the film's orientation, and disappear when the substrate is specifically oriented in zone axis a few nanometers from the interface (see the supplementary material, Figs. S8 and S9). Overall, a

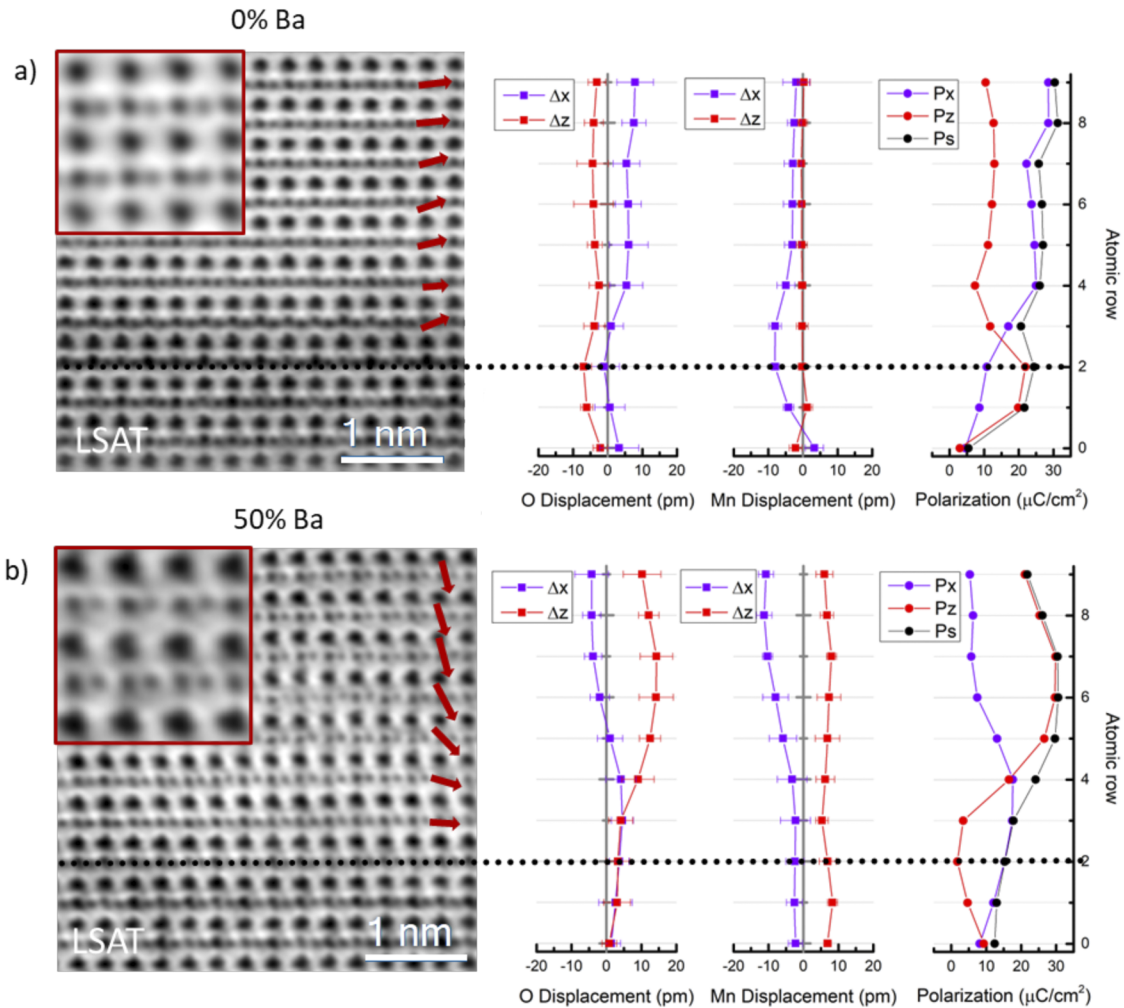


FIG. 2. ABF-STEM images of cross-sectional specimens of (a) $\text{SrMnO}_3/\text{LSAT}$ (001) and (b) $\text{Sr}_{0.5}\text{Ba}_{0.5}\text{MnO}_{3-\delta}/\text{LSAT}$ (001) viewed along the $\langle 110 \rangle$ direction. The insets show magnified images of the specimens, and the arrows represent the average magnitude and orientation of the spontaneous polarization of each atomic row of the film. Out-of-plane polar displacements are dominant in the $\text{Sr}_{0.5}\text{Ba}_{0.5}\text{MnO}_{3-\delta}$ film, while mostly in-plane polar shifts emerge in SrMnO_3 . The O and Mn out-of-plane (ΔZ) and in-plane (ΔX) shifts shown in both figures are visualized in the corresponding displacement plots. The average in-plane (P_x), out-of-plane (P_z) and overall (P_s) spontaneous polarization of the crystal cells across the thickness of the films are shown in the polarization plot.

spontaneous polarization with a maximum value of $30 \mu\text{C}/\text{cm}^2$ is present in the two films, which is in the range of polarization values predicted in SrMnO_3 for moderate tensile strain similar to the 1.7% nominal value of films grown on LSAT.²² It is worth noting that in the case of the SrMnO_3 film, the spontaneous polarization is predominantly in-plane, while in $\text{Sr}_{0.5}\text{Ba}_{0.5}\text{MnO}_{3-\delta}$ films out-of-plane polarization dominates, as illustrated with the arrows overlay on the ABF-STEM images of Fig. 2. Indeed, this result is the first experimental evidence of out-of-plane polar displacements induced in compressively strained films in this family of compounds.

The very different critical thicknesses for strain relaxation of the three compositions and the inhomogeneous polar states found in the ultrathin (10 nm) films of SrMnO_3 ³⁰ led us to study the effect of Ba content in films with optimized, subcritical thickness

values, different for each composition. However, size effects related to reduced thickness can have a significant impact on the structural and electrical properties of ferroelectric films through strain variation and screening of polarization at the interface, which can drastically affect the domain wall structure, polarization, switching, and imprint phenomena.^{36–38} In order to distinguish the possible impact of thickness from that of stoichiometry, we have analyzed the influence of oxygen content for the same Ba doping in specimens with constant thickness.

B. Oxygen stoichiometry

The formation of oxygen vacancies affects the physical properties of SrMnO_3 thin films, such as conductivity²³ and magnetic

order.³⁹ In $\text{Sr}_{1-x}\text{Ba}_x\text{MnO}_{3-\delta}$ ($x \geq 0.4$), oxygen vacancies emerge even at high annealing oxygen pressures as shown in other experimental works, mainly due to the increased chemical pressure.^{40,41} Lattice distortions induced by epitaxial strain are also bound to influence the oxygen stoichiometry⁴² in SBMO films. Indeed, it could also be engineered by modifying the temperature and oxygen pressure during growth and post-growth annealing, as has been shown in the bulk.⁴¹ Thus, we analyzed the influence of oxygen content on the polar states of oxygen-deficient $\text{Sr}_{0.6}\text{Ba}_{0.4}\text{MnO}_{3-\delta}$ films, which show a value of tensile strain near the threshold ($c/a = 1$) toward compressive strain (see Table II), by varying the temperature and oxygen pressure of the annealing. We avoided using $\text{Sr}_{0.5}\text{Ba}_{0.5}\text{MnO}_{3-\delta}$ as an agent to study the effect of oxygen vacancies since it was highly metastable and susceptible to oxygen content changes (see Fig. S3 in the supplementary material).

A detailed study was performed on two $\text{Sr}_{0.6}\text{Ba}_{0.4}\text{MnO}_{3-\delta}$ films synthesized with the same growth conditions but annealed at 550 °C, 400 Torr O_2 , and 650 °C, 300 Torr O_2 for 1 h, respectively (parameters that are different from the ones of the optimized film discussed in Sec. II A). The thickness was constrained to 12 nm, which

is again below the critical value reported by Langenberg *et al.*²⁹ It is noteworthy that the impact of the different annealing conditions (temperature and pressure) is visible in the XRD symmetric $\theta/2\theta$ scans shown in Fig. 3(a). The 002 main reflection of the film annealed at 550 °C and 400 Torr O_2 appears at a higher 2θ value than the LSAT 002 reflection, very similar to the optimized film (see Fig. 1), while that of the film annealed at 650 °C, 300 Torr O_2 appears at a 2θ angle lower than the substrate's one. The resulting out-of-plane lattice parameters of the films were 3.85 ± 0.01 Å and 3.89 ± 0.01 Å for annealing pressures of 400 and 300 Torr, respectively. These values indicate that decreasing the oxygen pressure and increasing the temperature during annealing causes the enlargement of the out-of-plane lattice parameter, and thus the cell volume. More importantly, the consequence of changing the annealing conditions is the transition from a tensile strained film ($c/a < 1$) in a highly oxidizing atmosphere to a compressively strained structure ($c/a > 1$) in more reducing conditions.

Electron energy loss spectroscopy (EELS) analysis has been carried out to quantify the combined influence of different annealing temperature and pressure on the number of oxygen vacancies (δ)

TABLE II. Annealing conditions and main structural parameters of the 40% Ba films whose polar distortions have been tuned by the annealing conditions: annealing temperature (T_{ann}), annealing O_2 pressure (P_{ann}), thickness (t), out-of-plane lattice parameter (c), out-of-plane strain (ϵ_{zz}) calculated as $100 \times (c_{\text{film}} - c_{\text{bulk}})/c_{\text{bulk}}$, in-plane lattice parameter (a), in-plane strain (ϵ_{xx}) calculated as $100 \times (a_{\text{film}} - a_{\text{bulk}})/a_{\text{bulk}}$, ratio between out-of-plane and in-plane lattice parameter (c/a), and cell volume (V).

x	T_{ann} (°C)	P_{ann} (Torr)	t (nm)	c (Å)	ϵ_{zz}	a (Å)	ϵ_{xx}	c/a	V (Å ³)
0.4	550	400	12	3.83(1)	-0.6%	3.868	+0.3%	0.993(3)	57.3(3)
0.4	650	300	12	3.89(1)	+1.0%	3.868	+0.3%	1.010(4)	58.3(3)

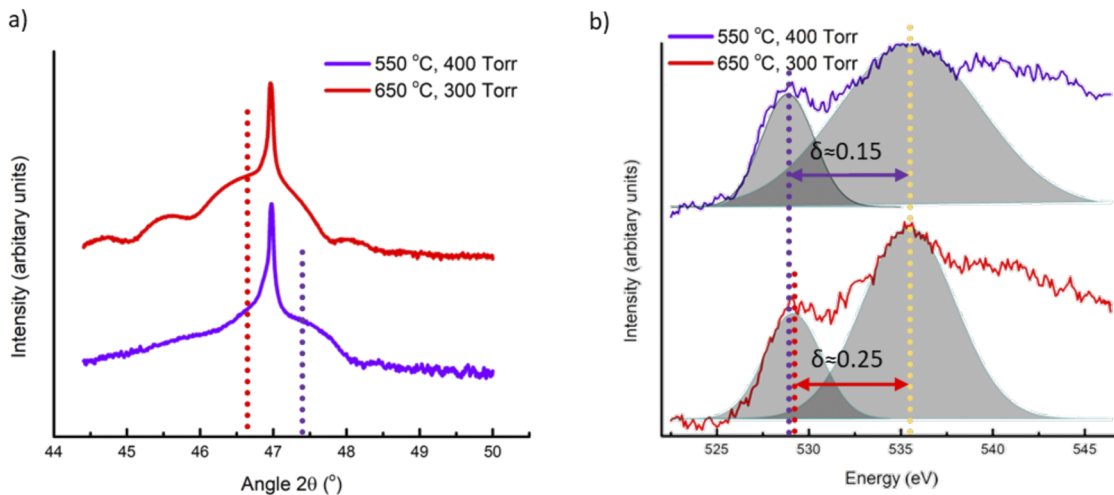


FIG. 3. (a) Symmetric $\theta/2\theta$ scans of epitaxial $\text{Sr}_{0.6}\text{Ba}_{0.4}\text{MnO}_{3-\delta}$ films grown on LSAT with low oxygen content (annealed at 650 °C, 300 Torr O_2) and high oxygen content (annealed at 550 °C, 400 Torr O_2). The position of the main peak of the film (dashed lines) moves toward smaller 2θ angles (out-of-plane lattice parameter $c = 3.894 \pm 0.008$ Å) in the case of low oxygen content due to the enlargement of the out-of-plane lattice parameter as a result of the higher concentration of oxygen vacancies. The out-of-plane lattice parameter of the high oxygen content film is $c = 3.832 \pm 0.007$ Å. (b) EELS spectra of the O K edge acquired in the vicinity of 530 eV from the $\text{Sr}_{0.6}\text{Ba}_{0.4}\text{MnO}_{3-\delta}$ films shown in (a). Low oxygen content ($\delta \approx 0.25$) spectrum is shown in red and high oxygen content ($\delta \approx 0.15$) in purple. 1D Gaussian fits of the pre-peak (~ 529 eV) and the main peak (~ 536 eV) of the O- K edge fine structure are plotted. The dashed lines indicate the center of the peaks which were used to estimate the Mn valence of the films.

by estimating the Mn valence.⁴³ The experimental O–K edge of the two aforementioned $\text{Sr}_{0.6}\text{Ba}_{0.4}\text{MnO}_{3-\delta}$ films is depicted in Fig. 3(b), together with the Gaussian fits used to calculate the Mn valence (as described in the Methods section). The estimated values of the Mn valence are $+3.69 \pm 0.05$ ($\delta \approx 0.15 \pm 0.01$) and $+3.51 \pm 0.05$ ($\delta \approx 0.25 \pm 0.01$) for the films with high and low oxygen pressure annealing,

respectively. Therefore, the $\text{Sr}_{0.6}\text{Ba}_{0.4}\text{MnO}_{2.75}$ film annealed at 650°C , 300 Torr O_2 accommodates more oxygen vacancies than the $\text{Sr}_{0.6}\text{Ba}_{0.4}\text{MnO}_{2.85}$ film annealed at 550°C and 400 Torr O_2 , which is in agreement with the evolution of their out-of-plane lattice parameter deduced from Fig. 3(a). The lower average Mn valence, driven by the formation of oxygen vacancies, implies a larger ionic radius,

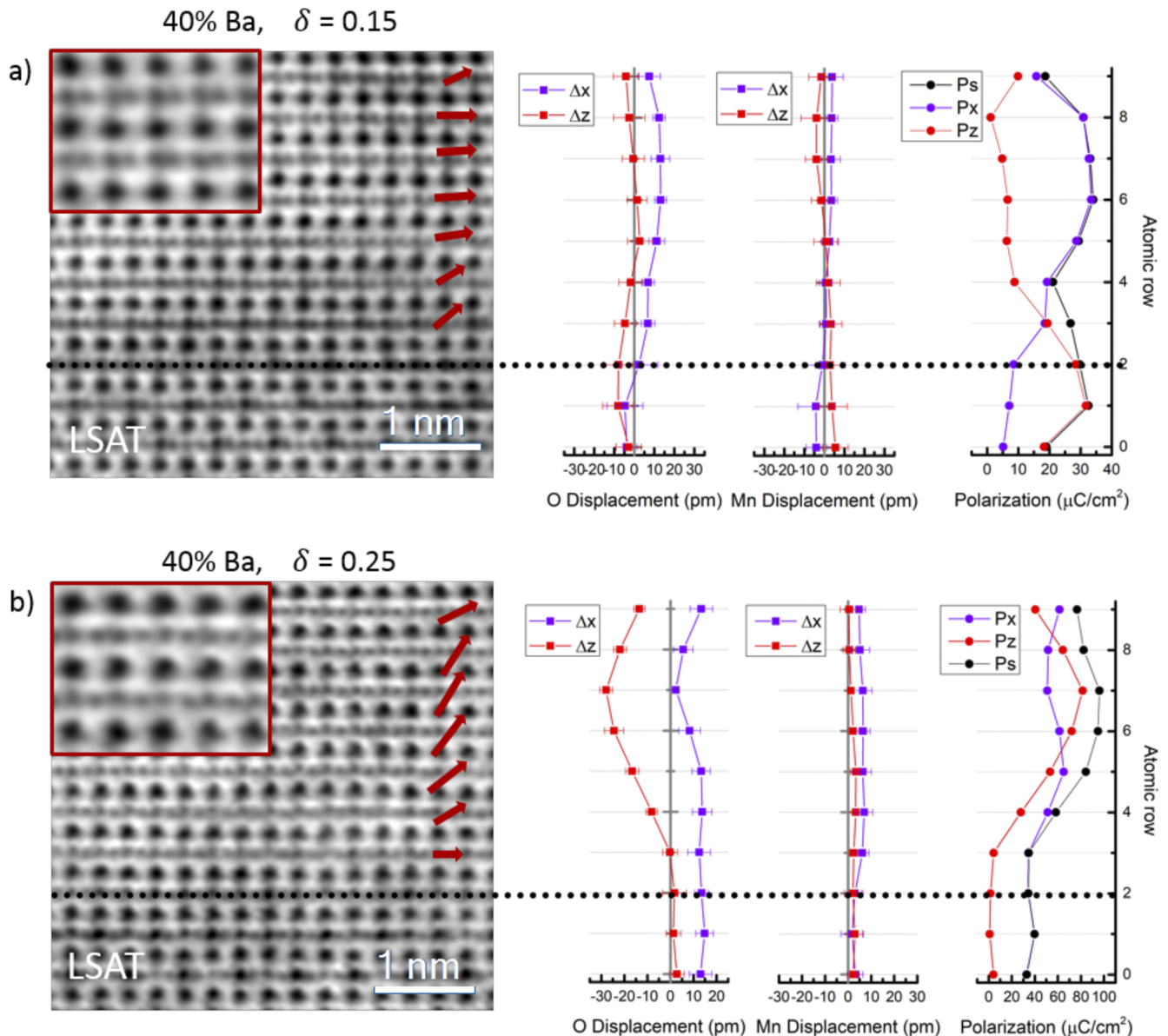


FIG. 4. ABF-STEM images of cross-sectional specimen of the (a) $\text{Sr}_{0.6}\text{Ba}_{0.4}\text{MnO}_{2.85}$ and (b) $\text{Sr}_{0.6}\text{Ba}_{0.4}\text{MnO}_{2.75}$ grown on LSAT (001) and annealed at (a) 400 Torr, 550°C and (b) 300 Torr, 650°C for 1 h, viewed along the (110) direction. The insets show a magnified image of the specimen, and the arrows indicate the average magnitude and orientation of the spontaneous polarization of each atomic row of the film. The O and Mn out-of-plane (ΔZ) and in-plane (ΔX) displacements shown in both figures are visualized in the corresponding displacement plots. Out-of-plane polarization is dominant in the $\text{Sr}_{0.6}\text{Ba}_{0.4}\text{MnO}_{2.75}$ film, while in-plane polarization dictates in the case of the more oxidized $\text{Sr}_{0.6}\text{Ba}_{0.4}\text{MnO}_{2.85}$ film. The estimated average in-plane (P_x), out-of-plane (P_z) and overall (P_s) spontaneous polarization of the crystal cells across the thickness of the films are shown in the polarization plot.

which increases the out-of-plane lattice parameter and the cell volume. Our results follow the description of Dabrowski *et al.*,⁴¹ where the valence of the $\text{Mn}^{+4-2\delta}$ ion, its radius, and therefore the cell volume can be adjusted as a function of the oxygen vacancies.

Oxygen content also drastically changes the polar order of $\text{Sr}_{0.6}\text{Ba}_{0.4}\text{MnO}_{3-\delta}$ thin films. A quantitative analysis of the polar displacements in ABF-STEM images of the same two $\text{Sr}_{0.6}\text{Ba}_{0.4}\text{MnO}_{3-\delta}$ films is shown in Fig. 4. Specifically, the $\text{Sr}_{0.6}\text{Ba}_{0.4}\text{MnO}_{2.85}$ sample encounters in-plane polar displacements of O of ~ 15 pm, qualitatively similar to those observed in the nearly stoichiometric parent compound SrMnO_3 [Fig. 2(a)]. In contrast, out-of-plane shifts of the equatorial oxygen positions up to ~ 28 pm are detected in the $\text{Sr}_{0.6}\text{Ba}_{0.4}\text{MnO}_{2.75}$ sample. Thus, a change of polar displacements from in-plane to out-of-plane can be induced purely by modifying the oxygen stoichiometry at a constant thickness.

Quantitative analysis of the ABF image of the $\text{Sr}_{0.6}\text{Ba}_{0.4}\text{MnO}_{2.85}$ film [see Fig. 4(a)] shows a spontaneous polarization of about $30 \mu\text{C}/\text{cm}^2$ arising mostly from the contribution of oxygen in-plane shifts, similar to tensile-strained in-plane polar SBMO films shown elsewhere.^{30,31} A radically different behavior is observed in the $\text{Sr}_{0.6}\text{Ba}_{0.4}\text{MnO}_{2.75}$ film displayed in Fig. 4(b), where spontaneous polarization up to $95 \mu\text{C}/\text{cm}^2$ owing to large out-of-plane and in-plane shifts of the oxygen atoms has been computed. This value is remarkably higher than that observed in the rest of the films studied here and is in good agreement with those estimated by Guzmán *et al.* using a similar methodology in oxygen-deficient SrMnO_3 films.³⁰ In that case, out-of-plane polar rotations were observed associated with a concomitant gradient of oxygen vacancies and strain across the film thickness.³⁰ This might be an indication that highly oxygen-deficient SBMO films also favor larger polarization values with respect to stoichiometric ones. It also suggests that small variations of the atomic displacements observed in the ABF images of the films could be associated with small local variations in the oxygen stoichiometry.³⁰

Hence, these observations prove experimentally that, among the different demonstrations of how oxygen stoichiometry can influence the crystal structure and functional properties of oxide thin films, the polar axis of SBMO multiferroic thin films can also be switched from in-plane to out-of-plane orientation by tuning the concentration of oxygen vacancies.

C. Synergistic effects

A theoretical study from Marthinsen *et al.*³³ states that the expansion of the cell volume promotes polar distortions as a consequence of the decrease in the Coulomb repulsion between the displaced Mn cation and the O anions. However, in the case of tensile strain, polar distortions compete with the formation of oxygen vacancies, which can suppress polarization.³³ Therefore, by gaining control over the oxygen vacancies and Ba content, we can stimulate polar distortions in SBMO and selectively induce either in-plane or out-of-plane polar displacements.

Intriguingly, the emergence of out-of-plane polar displacements in the compressively strained $\text{Sr}_{0.6}\text{Ba}_{0.4}\text{MnO}_{2.75}$ film grown on LSAT is an example of a synergistic effect between Ba content and oxygen stoichiometry. High Ba content ($x = 0.4$) and low oxygen content ($\delta = 0.25$) promote the emergence of compressive strain and trigger the displacement of oxygen atomic columns out-of-plane, as shown in Fig. 4.

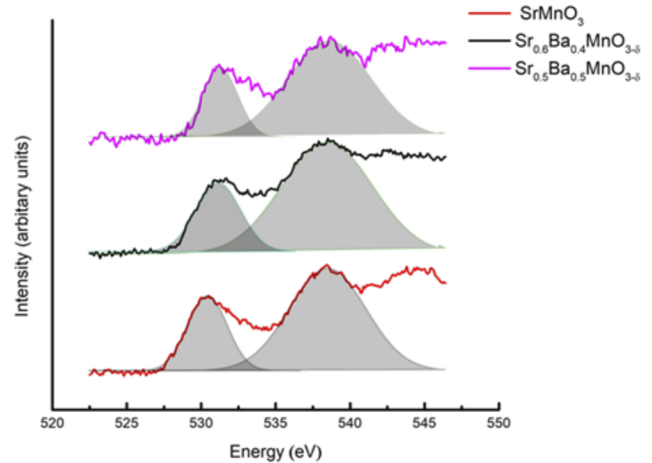


FIG. 5. EELS spectra of the O K edge acquired in the vicinity of 530 eV from the $\text{Sr}_{1-x}\text{Ba}_x\text{MnO}_{3-\delta}$ films with 0%, 40% and 50% Ba content. The estimated Mn valence in the $\text{SrMnO}_{3-\delta}$ film was $+4.02 \pm 0.03$, while those of $\text{Sr}_{0.6}\text{Ba}_{0.4}\text{MnO}_{3-\delta}$ and $\text{Sr}_{0.5}\text{Ba}_{0.5}\text{MnO}_{3-\delta}$ films were $+3.82 \pm 0.05$ and $+3.75 \pm 0.05$, respectively.

Finally, Ba content and oxygen stoichiometry are not mutually independent parameters. Substituting Sr with Ba at the A sites causes an increase in the average ionic radius at the A position, inducing a rise in the cell volume that in turn favors the formation of oxygen vacancies. From the energy point of view, Ba doping decreases the oxygen vacancy formation energy in epitaxial SBMO films, and inevitably more oxygen vacancies may emerge, as explained elsewhere.⁴⁴⁻⁴⁶ This interplay between Ba and O stoichiometry is evidenced in Fig. 5, which shows O-K EELS spectra collected from the optimal films shown in Fig. 1 with different Ba content ($x = 0, 0.4, \text{ and } 0.5$). The experimental value of Mn valence in the parent compound SrMnO_3 was $+4.02 \pm 0.03$, which indicates a fully stoichiometric crystal. On the other hand, in high Ba content samples, the highest Mn valence we reported was $+3.82 \pm 0.05$ for $x = 0.4$ and $+3.75 \pm 0.05$ for $x = 0.5$, respectively.

III. CONCLUSIONS

In this work, we evidence a chemistry-mediated route to engineer the polar distortions of strained single-crystalline $\text{Sr}_{1-x}\text{Ba}_x\text{MnO}_3$ thin films. Once the in-plane lattice parameter of the films is fixed by the biaxial epitaxial strain of the LSAT (001) substrate, the magnitude and orientation of the polar displacements observed are tailored by modifying the Ba doping and oxygen stoichiometry through post-growth annealing. The combined effect of Ba doping, oxygen vacancies and epitaxy directs the polar displacements out-of-plane in a compressively strained $\text{Sr}_{0.5}\text{Ba}_{0.5}\text{MnO}_{3-\delta}$ films, while the stoichiometric parent compound SrMnO_3 shows in-plane displacements driven by tensile strain as a function of the Ba composition and growth parameters. Last but not least, we observe that the polar displacements can be switched from in-plane to out-of-plane by modulating the oxygen stoichiometry alone for a given Ba doping, as large out-of-plane polarization emerges in highly oxygen deficient $\text{Sr}_{0.6}\text{Ba}_{0.4}\text{MnO}_{2.75}$ thin films grown on LSAT. We attribute this effect to the rise of Mn^{3+} ions under reducing

conditions, which contribute to the increase in the cell volume and, thus, the out-of-plane lattice parameter in these fully coherent, epitaxial films. In summary, our findings show that the cooperative action of tailored stoichiometry and epitaxial strain is critical for the emergence and control of polar states in this family of compounds, and the impact of growth conditions on the crystal and polar displacements of strained $\text{Sr}_{1-x}\text{Ba}_x\text{MnO}_3$ enables tailoring of polarization when the film is subjected to boundary conditions imposed by epitaxial growth. Particularly, the oxygen content invokes considerable changes in the crystalline and electronic properties of the films, as it is shown elsewhere.²³ In this respect, our work paves the way for understanding the impact of growth parameters on $\text{Sr}_{1-x}\text{Ba}_x\text{MnO}_{3-\delta}$ films and other compounds sharing equivalent chemical and crystalline structures.

This approach opens new possibilities for the design of a new concept of multiferroic films and heterostructures in which tailoring the polar distortions by chemical doping enables a broader control of the ferroic order and the magnetoelectric coupling of thin films, even grown with the same nominal stoichiometry of the target. Finally, rich and unexpected nanoscale phenomena may emerge from the design and study of chemistry-mediated heteropolar multilayers and motivate new approaches for the integration of ferroelectrics and multiferroics in future nanoelectronics.

IV. EXPERIMENTAL SECTION

Epitaxial $\text{Sr}_{1-x}\text{Ba}_x\text{MnO}_{3-\delta}$ thin films with compositions $x = 0, 0.4,$ and 0.5 and thicknesses in the range $7\text{--}18$ nm were deposited on single crystalline (001)-oriented $(\text{LaAlO}_3)_{0.3}(\text{Sr}_2\text{TaAlO}_6)_{0.7}$ (LSAT) substrates from Crystal GmbH. The films were grown by pulsed laser deposition (PLD) using a KrF excimer laser, a fluence of 1 J/cm², and a pulse repetition rate of 10 Hz. The substrate temperature was set at 850 °C, with cooling/heating rates of 10 °C/min. In the case of SrMnO_3 the oxygen pressure during growth was set at 50 mTorr, while SBMO films with $x = 0.4, 0.5$ were grown at 0.05 mTorr to reduce the Mn valence, increasing its ionic radius and thus favoring the stabilization of the pseudocubic perovskite phase. *In situ* post-growth annealing was performed to control the oxygen stoichiometry. SrMnO_3 epitaxial thin films were annealed at 800 °C for 30 min at O_2 pressures ranging from 300 to 500 Torr. $\text{Sr}_{0.6}\text{Ba}_{0.4}\text{MnO}_{3-\delta}$ films were annealed for 1 h at temperatures ranging from 250 to 750 °C and O_2 pressures between 300 and 590 Torr. $\text{Sr}_{0.5}\text{Ba}_{0.5}\text{MnO}_{3-\delta}$ films were annealed for 1 h at 650 °C in a range of pressures between 350 and 550 Torr.

The crystal structure and thickness of the films were studied by X-ray diffraction (XRD) and X-ray reflectivity (XRR), while atomic-level analysis of the SBMO films was performed by scanning transmission electron microscopy (STEM) (see Sec. IV in the supplementary material). The atomic displacements were measured from the ABF and HAADF images, and finally the film polarization was evaluated (see Fig. S6 in the supplementary material).

Electron energy loss spectroscopy (EELS) in STEM was performed to assess the oxygen content of the films. The fine structure of the background-subtracted O–K edge was fitted to a double Gaussian to quantify the Mn valence following the procedure described by Varela *et al.*⁴³ In-plane deformation maps out of HAADF-STEM images were calculated using geometric phase analysis (GPA) to study locally the quality of substrate-induced strain in the films.

Lamella specimens for STEM were prepared with an FEI Helios 650 Dual Beam system and the final thinning was performed by low-angle Ar^+ ion polishing in a Fischione 1010 ion mill. Energy dispersive x-ray analysis was carried out to estimate the chemical composition of the films with respect to the nominal composition of the targets.

SUPPLEMENTARY MATERIAL

Additional structural (XRD and STEM) and chemical x-ray microanalysis, a detailed description of the STEM image analysis and calculation of polarization images, including the LSAT substrate, and further details on the experimental conditions are provided in the supplementary material.

ACKNOWLEDGMENTS

We acknowledge the research Project No. PID2020-112914RB-I00 funded by Grant No. MCIN/AEI/10.13039/501100011033. This work was funded from Regional Gobierno de Aragón through Project Nos. E13_23R and E28_23R, including FEDER funding and from the EU Horizon 2020 programme under the Marie Skłodowska-Curie Grant Agreement No. 861153 MANIC, and under the Grant Agreement No. 823717-ESTEEM3. The authors acknowledge the use of instrumentation as well as the technical advice provided by the National Facility ELECMI ICTS, node “Laboratorio de Microscopías Avanzadas (LMA)” at “Universidad de Zaragoza”.

We acknowledge Javier Blasco from INMA-CSIC (Zaragoza, Spain) for the synthesis of the PLD targets and Christophe Gatel from CEMES-CNRS (Toulouse, France) for the STEM image acquisition and drift correction scripts.

AUTHOR DECLARATIONS

Conflict of Interest

The authors have no conflicts to disclose.

Author Contributions

Panagiotis Koutsogiannis: Data curation (equal); Formal analysis (equal); Software (equal); Writing – original draft (equal). **Pedro A. Algarabel:** Investigation (supporting); Supervision (supporting); Writing – review & editing (equal). **José A. Pardo:** Conceptualization (equal); Funding acquisition (equal); Supervision (equal); Writing – review & editing (equal). **César Magén:** Conceptualization (lead); Funding acquisition (lead); Methodology (equal); Project administration (lead); Supervision (lead); Validation (lead); Writing – review & editing (equal).

DATA AVAILABILITY

The data that support the findings of this study are available from the corresponding author upon request.

REFERENCES

- 1M. Fiebig, T. Lottermoser, D. Meier, and M. Trassin, “The evolution of multiferroics,” *Nat. Rev. Mater.* **1**(8), 16046 (2016).
- 2N. A. Spaldin, “Multiferroics beyond electric-field control of magnetism,” *Proc. R. Soc. A* **476**(2233), 20190542 (2020).

- ³J. F. Scott, *Nat. Mater.* **6**, 256–257 (2007).
- ⁴M. Bibes and A. Barthélémy, “Multiferroics: Towards a magnetoelectric memory,” *Nat. Mater.* **7**(6), 425–426 (2008).
- ⁵M. Trassin, “Low energy consumption spintronics using multiferroic heterostructures,” *J. Phys.: Condens. Matter* **28**(3), 033001 (2016).
- ⁶M. A. Jalaja and S. Dutta, “Ferroelectrics and multiferroics for next generation photovoltaics,” *Adv. Mater. Lett.* **6**(7), 568–584 (2015).
- ⁷H. Wu, A. Tatarenko, M. I. Bichurin, and Y. Wang, “A multiferroic module for biomechanical energy harvesting,” *Nano Energy* **83**, 105777 (2021).
- ⁸K. Guo, X. Wang, R. Zhang, Z. Fu, L. Zhang, G. Ma, and C. Deng, “Multiferroic oxide BFCNT/BFCO heterojunction black silicon photovoltaic devices,” *Light Sci. Appl.* **10**, 201 (2021).
- ⁹B. Sun, G. Zhou, L. Sun, H. Zhao, Y. Chen, F. Yang, Y. Zhao, and Q. Song, “ABO₃ multiferroic perovskite materials for memristive memory and neuromorphic computing,” *Nanoscale Horiz.* **6**(12), 939–970 (2021).
- ¹⁰D. G. Schlom, L.-Q. Chen, C.-B. Eom, K. M. Rabe, S. K. Streiffer, and J.-M. Triscone, “Strain tuning of ferroelectric thin films,” *Annu. Rev. Mater. Res.* **37**(1), 589–626 (2007).
- ¹¹L. W. Martin and A. M. Rappe, “Thin-film ferroelectric materials and their applications,” *Nat. Rev. Mater.* **2**(2), 16087 (2016).
- ¹²J. H. Haeni, P. Irvin, W. Chang, R. Uecker, P. Reiche, Y. L. Li, S. Choudhury, W. Tian, M. E. Hawley, B. Craigo, A. K. Tagantsev, X. Q. Pan, S. K. Streiffer, L. Q. Chen, S. W. Kirchoefer, J. Levy, and D. G. Schlom, “Room-temperature ferroelectricity in strained SrTiO₃,” *Nature* **430**(7001), 758–761 (2004).
- ¹³J. H. Lee, L. Fang, E. Vlahos, X. Ke, Y. W. Jung, L. F. Kourkoutis, J. W. Kim, P. J. Ryan, T. Heeg, M. Roeckerath, V. Goian, M. Bernhagen, R. Uecker, P. C. Hammel, K. M. Rabe, S. Kamba, J. Schubert, J. W. Freeland, D. A. Muller, C. J. Fennie, P. Schiffer, V. Gopalan, E. Johnston-Halperin, and D. G. Schlom, “A strong ferroelectric ferromagnet created by means of spin-lattice coupling,” *Nature* **466**(7309), 954–958 (2010).
- ¹⁴M. Tyunina, J. Narkilähti, M. Plekh, R. Oja, R. M. Nieminen, A. Dejneka, and V. Trepakov, “Evidence for strain-induced ferroelectric order in epitaxial thin-film KTaO₃,” *Phys. Rev. Lett.* **104**(22), 227601 (2010).
- ¹⁵O. Diéguez, K. M. Rabe, and D. Vanderbilt, “First-principles study of epitaxial strain in perovskites,” *Phys. Rev. B* **72**(14), 144101 (2005).
- ¹⁶G. Giovannetti, S. Kumar, C. Ortix, M. Capone, and J. van den Brink, “Microscopic origin of large negative magneto-electric coupling in Sr_{1/2}Ba_{1/2}MnO₃,” *Phys. Rev. Lett.* **109**(10), 107601 (2012).
- ¹⁷M. D. Glinchuk, E. A. Eliseev, Y. Gu, L. Q. Chen, V. Gopalan, and A. N. Morozovska, “Electric-field induced ferromagnetic phase in paraelectric antiferromagnets,” *Phys. Rev. B* **89**(1), 014112 (2014).
- ¹⁸T. Birol, N. A. Benedek, H. Das, A. L. Wysocki, A. T. Mulder, B. M. ABBETT, E. H. Smith, S. Ghosh, and C. J. Fennie, “The magnetoelectric effect in transition metal oxides: Insights and the rational design of new materials from first principles,” *Curr. Opin. Solid State Mater. Sci.* **16**(5), 227–242 (2012).
- ¹⁹J. Briatico, B. Alascio, R. Allub, A. Butera, A. Caneiro, M. T. Causa, and M. Tovar, “Double-exchange interaction in electron-doped CaMnO_{3-δ} perovskites,” *Phys. Rev. B* **53**(21), 14020–14023 (1996).
- ²⁰T. Günter, E. Bousquet, A. David, P. Boullay, P. Ghosez, W. Prellier, and M. Fiebig, “Incipient ferroelectricity in 2.3% tensile-strained CaMnO₃ films,” *Phys. Rev. B* **85**(21), 214120 (2012).
- ²¹S. Bhattacharjee, E. Bousquet, and P. Ghosez, “Engineering multiferroism in CaMnO₃,” *Phys. Rev. Lett.* **102**(11), 117602 (2009).
- ²²J. H. Lee and K. M. Rabe, “Epitaxial-strain-induced multiferroicity in SrMnO₃ from first principles,” *Phys. Rev. Lett.* **104**(20), 207204 (2010).
- ²³C. Becher, L. Maurel, U. Aschauer, M. Lilienblum, C. Magén, D. Meier, E. Langenberg, M. Trassin, J. Blasco, I. P. Krug, P. A. Algarabel, N. A. Spaldin, J. A. Pardo, and M. Fiebig, “Strain-induced coupling of electrical polarization and structural defects in SrMnO₃ films,” *Nat. Nanotechnol.* **10**(8), 661–665 (2015).
- ²⁴J. W. Guo, P. S. Wang, Y. Yuan, Q. He, J. L. Lu, T. Z. Chen, S. Z. Yang, Y. J. Wang, R. Erni, M. D. Rossell, V. Gopalan, H. J. Xiang, Y. Tokura, and P. Yu, “Strain-induced ferroelectricity and spin-lattice coupling in SrMnO₃ thin films,” *Phys. Rev. B* **97**(23), 235135 (2018).
- ²⁵H. An, Y.-G. Choi, Y.-R. Jo, H. J. Hong, J.-K. Kim, O. Kwon, S. Kim, M. Son, J. Yang, J.-C. Park, H. Choi, J. Lee, J. Song, M. Ham, S. Ryu, Y. Kim, C. W. Bark, K.-T. Ko, B.-J. Kim, and S. Lee, “Experimental realization of strain-induced room-temperature ferroelectricity in SrMnO₃ films via selective oxygen annealing,” *NPG Asia Mater.* **13**(1), 69 (2021).
- ²⁶H. Sakai, J. Fujioka, T. Fukuda, D. Okuyama, D. Hashizume, F. Kagawa, H. Nakao, Y. Murakami, T. Arima, A. Q. R. Baron, Y. Taguchi, and Y. Tokura, “Displacement-type ferroelectricity with off-center magnetic ions in perovskite Sr_{1-x}Ba_xMnO₃,” *Phys. Rev. Lett.* **107**(13), 137601 (2011).
- ²⁷T. Negas, “The Ba_{1-y}Sr_yMnO_{3-x} system,” *J. Solid State Chem.* **6**(1), 136–150 (1973).
- ²⁸O. Chmaissem, B. Dabrowski, S. Kolesnik, J. Mais, D. E. Brown, R. Kruk, P. Prior, B. Pyles, and J. D. Jorgensen, “Relationship between structural parameters and the Néel temperature in Sr_{1-x}Ca_xMnO₃ (0 ≤ x ≤ 1) and Sr_{1-y}Ba_yMnO₃ (y ≤ 0.2),” *Phys. Rev. B* **64**(13), 134412 (2001).
- ²⁹E. Langenberg, R. Guzmán, L. Maurel, L. Martínez de Baños, L. Morellón, M. R. Ibarra, J. Herrero-Martín, J. Blasco, C. Magén, P. A. Algarabel, and J. A. Pardo, “Epitaxial stabilization of the perovskite phase in (Sr_{1-x}Ba_x)MnO₃ thin films,” *ACS Appl. Mater. Interfaces* **7**(43), 23967–23977 (2015).
- ³⁰R. Guzmán, L. Maurel, E. Langenberg, A. R. Lupini, P. A. Algarabel, J. A. Pardo, and C. Magén, “Polar-graded multiferroic SrMnO₃ thin films,” *Nano Lett.* **16**(4), 2221–2227 (2016).
- ³¹E. Langenberg, L. Maurel, N. Marcano, R. Guzmán, P. Štrichovanec, T. Prokscha, C. Magén, P. A. Algarabel, and J. A. Pardo, “Controlling the electrical and magnetoelectric properties of epitaxially strained Sr_{1-x}Ba_xMnO₃ thin films,” *Adv. Mater. Interfaces* **4**(9), 1–10 (2017).
- ³²E. Markiewicz, R. Bujakiewicz-Koronska, A. Budziak, A. Kalvane, and D. M. Nalecz, “Impedance spectroscopy studies of SrMnO₃, BaMnO₃ and Ba_{0.5}Sr_{0.5}MnO₃ ceramics,” *Phase Transitions* **87**(10–11), 1060–1072 (2014).
- ³³A. Marthinsen, C. Faber, U. Aschauer, N. A. Spaldin, and S. M. Selbach, “Coupling and competition between ferroelectricity, magnetism, strain, and oxygen vacancies in AMnO₃ perovskites,” *MRS Commun.* **6**(3), 182–191 (2016).
- ³⁴N. A. Pertsev, A. G. Zembilgotov, and A. K. Tagantsev, “Effect of mechanical boundary conditions on phase diagrams of epitaxial ferroelectric thin films,” *Phys. Rev. Lett.* **80**(9), 1988–1991 (1998).
- ³⁵S. D. Findlay, N. Shibata, H. Sawada, E. Okunishi, Y. Kondo, and Y. Ikuhara, “Dynamics of annular bright field imaging in scanning transmission electron microscopy,” *Ultramicroscopy* **110**(7), 903–923 (2010).
- ³⁶A. K. Tagantsev and G. Gerra, “Interface-induced phenomena in polarization response of ferroelectric thin films,” *J. Appl. Phys.* **100**(5), 051607 (2006).
- ³⁷S. V. Kalinin, Y. Kim, D. D. Fong, and A. N. Morozovska, “Surface-screening mechanisms in ferroelectric thin films and their effect on polarization dynamics and domain structures,” *Rep. Prog. Phys.* **81**(3), 036502 (2018).
- ³⁸A. K. Tagantsev, L. Eric Cross, and J. Fousek, *Domains in Ferroic Crystals and Thin Films* (Springer, 2010).
- ³⁹L. Maurel, N. Marcano, T. Prokscha, E. Langenberg, J. Blasco, R. Guzmán, A. Suter, C. Magén, L. Morellón, M. R. Ibarra, J. A. Pardo, and P. A. Algarabel, “Nature of antiferromagnetic order in epitaxially strained multiferroic SrMnO₃ thin films,” *Phys. Rev. B* **92**(2), 024419 (2015).
- ⁴⁰L. Rørmørk, A. B. Mørch, K. Wiik, S. Stølen, and T. Grande, “Enthalpies of oxidation of CaMnO_{3-δ}, Ca₂MnO_{4-δ} and SrMnO_{3-δ}—Deduced redox properties,” *Chem. Mater.* **13**(11), 4005–4013 (2001).
- ⁴¹B. Dabrowski, O. Chmaissem, J. Mais, S. Kolesnik, J. D. Jorgensen, and S. Short, “Tolerance factor rules for Sr_{1-x-y}Ca_xBa_yMnO₃ perovskites,” *J. Solid State Chem.* **170**(1), 154–164 (2003).
- ⁴²E. Langenberg, L. Maurel, G. Antorrena, P. A. Algarabel, C. Magén, and J. A. Pardo, “Relaxation mechanisms and strain-controlled oxygen vacancies in epitaxial SrMnO₃ films,” *ACS Omega* **6**(20), 13144–13152 (2021).
- ⁴³M. Varela, M. P. Oxley, W. Luo, J. Tao, M. Watanabe, A. R. Lupini, S. T. Pantelides, and S. J. Pennycook, “Atomic-resolution imaging of oxidation states in manganites,” *Phys. Rev. B* **79**(8), 085117 (2009).

⁴⁴K. P. Kelley, A. N. Morozovska, E. A. Eliseev, V. Sharma, D. E. Yilmaz, A. C. T. van Duin, P. Ganesh, A. Borisevich, S. Jesse, P. Maksymovych, N. Balke, S. V. Kalinin, and R. K. Vasudevan, "Oxygen vacancy injection as a pathway to enhancing electromechanical response in ferroelectrics," *Adv. Mater.* **34**(2), 2106426 (2022).

⁴⁵H. Elangovan, M. Barzilay, J. Huang, S. Liu, S. Cohen, and Y. Ivry, "Engineering individual oxygen vacancies: Domain-wall conductivity and controllable topological solitons," *ACS Nano* **15**(8), 13380–13388 (2021).

⁴⁶Y. Noguchi, H. Matsuo, Y. Kitanaka, and M. Miyayama, "Ferroelectrics with a controlled oxygen-vacancy distribution by design," *Sci. Rep.* **9**(1), 4225 (2019).